



NiMo catalysts supported on Mn-Al₂O₃ for dibenzothiophene hydrodesulfurization application

A. López-Benítez^a, G. Berhault^b, A. Guevara-Lara^{a,*}

^a Área Académica de Química, Universidad Autónoma del Estado de Hidalgo, Carr. Pachuca-Tulancingo Km. 4.5, C.P. 42184 Pachuca, Hidalgo, Mexico

^b Institut de Recherches sur la Catalyse et l'Environnement de Lyon, CNRS/Université Lyon I, 02 av. Albert Einstein, 69100 Villeurbanne, France

ARTICLE INFO

Article history:

Received 2 March 2017

Received in revised form 13 April 2017

Accepted 21 April 2017

Available online 1 May 2017

Keywords:

MnO-Al₂O₃ support

Mixed oxides

Sol-gel

Hydrodesulfurization

ABSTRACT

Modification of the traditional Al₂O₃ support through addition of manganese to Al₂O₃ mixed Mn-Al oxides was herein envisaged to obtain highly active NiMo catalysts for hydrodesulfurization application. The effect of adding manganese was determined considering different Mn-Al₂O₃ supports synthesized using a sol-gel approach. The manganese-containing supports were furthermore impregnated with Ni(NO₃)₂ + (NH₄)₆Mo₇O₂₄ aqueous solutions at pH = 9 and characterized at their oxide state using UV-vis diffuse reflectance and Raman spectroscopies after drying and calcination steps. NiMo/Mn-Al₂O₃ catalysts were also characterized at the sulfide state mainly by X-ray photoelectron spectroscopy (XPS) and transmission electron microscopy (TEM). Finally, the sulfide catalysts were evaluated in the hydrodesulfurization of dibenzothiophene.

Results show that the oxidation state of manganese species directly influences the nature of the Mo oxide species and their interaction with the Al₂O₃ support. At low Mn content (up to 0.5 mol% Mn as MnO), Mn²⁺ species leads to weaker interaction with the support and a higher intrinsic activity of the NiMoS species. However, these promoted sites are also formed in a lower amount than without adding Mn to the support. At too high manganese content (≥2 mol% Mn as MnO), Mn³⁺ species are formed and react with Ni to form a spinel phase decreasing the proportion of promoted phase to be formed after sulfidation. The highest activity is therefore observed at an intermediate Mn content of 1 mol% for which a higher intrinsic activity resulting from weaker support interaction and higher sulfidation rate combine together to achieve highly active NiMo HDS catalysts.

© 2017 Elsevier B.V. All rights reserved.

1. Introduction

Nowadays, the removal of sulfur from petroleum feedstocks remains an important environmental problem leading consequently to the introduction of increasingly stricter governmental regulations controlling the emission of pollutants by vehicles [1]. Hydrodesulfurization (HDS) is one of the most important steps in refinery operations that allows to remove sulfur from petroleum feedstock through a catalytic process [2].

Catalysts commonly used in hydrodesulfurization consist of MoS₂ or WS₂ clusters promoted by Co or Ni and supported on γ-Al₂O₃ [3]. Among the different S-containing molecules present in feedstocks, dibenzothiophene (DBT) and alkyl-dibenzothiophenes are considered the most refractory molecules to be desulfurized and their presence limits the production of ultralow sulfur diesel

[4]. The development of more active catalysts is an effective way to increase HDS efficiency and to satisfy the increasing demand for ultralow sulfur diesel (<10 ppm) [2,5].

The preparation of HDS catalysts involves 4 important steps: (1) formation of Ni-Mo complex in the impregnation solution, (2) impregnation on a support and drying step, (3) calcination step, and (4) activation through sulfidation. In the impregnation solution, the formation of Ni-Mo complexes depends on the nature of the salts, additives, chelating agents and of the pH of impregnation solutions [6,7]. For example, Ni²⁺_(Td)/MoO₄²⁻ complex is formed in an aqueous solution of (NH₄)₆Mo₇O₂₄·6H₂O and Ni(NO₃)₂·6H₂O at pH = 9 while the Ni²⁺_(Oh)/Mo₇O₂₄⁶⁻ complex is formed with the same salts dissolved in water but at pH = 7 [8].

In the case of the impregnation step, metal-support interactions determine the nature of the Ni-Mo oxospecies formed on the catalyst [9]. On the other hand, temperatures used for drying and calcining can also influence activity. Calcination allows decomposing the precursors leading to oxospecies deposited on the support. Calcination can also impact other parameters such as the reducibil-

* Corresponding author.

E-mail address: guevaraa@uaeh.edu.mx (A. Guevara-Lara).

ity and the distribution of the metals in the final catalyst structure [10].

Catalyst activation consists in the conversion of the oxide species into sulfided phases with a reduction-sulfidation reaction using $\text{H}_2\text{S}/\text{H}_2$ mixture. In this process, metal-support interactions control the dispersion and morphology of the active phase [11]. Also, sulfidation influences the electronic and geometric properties of the active phase [12–14] which determine the final structure and activity of the HDS catalysts.

Topsøe et al. [15] explain that the activity of Mo sulfide catalysts promoted by Ni or Co depends on the formation of the called “Co-Mo-S” or “Ni-Mo-S” phases. In the CoMoS or NiMoS phases, the Ni or Co promoter atoms are located at the edge planes of MoS_2 layers. However, in some unwanted cases, the Ni or Co atoms also form inactive phases such as nickel sulfide or nickel aluminate that do not participate in improving the HDS activity.

A good control of the parameters influencing the preparation procedure is a strong prerequisite to achieve high hydrodesulfurization activity [6]. In this respect, it is necessary that the Ni-Mo interaction remains effective during the whole procedure of catalyst preparation. This can be obtained through catalyst characterization at each step of the catalyst preparation in order to control and to check the nature of Ni-Mo species and of the degree of support interaction responsible for the overall activity.

On the other hand, the necessity of more active and selective HDS catalysts implies to obtain more and more efficient supported catalytic systems. Therefore, the synthesis of highly active HDS catalysts can be based on the modification of the active phase and/or of the support. One interesting option is the modification or substitution of the traditional Al_2O_3 support in order to achieve mixed oxides. Synthesis of new mixed oxides containing alumina provides an easy way to prepare catalysts with high surface area, high thermal stability and suitable mechanical properties as requested for hydrodesulfurization supports. Moreover, mixing two components allows to take advantage of the favorable characteristics coming from both elements as exemplified in a large extent in the literature (e.g. Ga- Al_2O_3 , B- Al_2O_3 , TiO_2 - Al_2O_3 , SBA-15-Al, P_2O_5 - Al_2O_3 , MgO - Al_2O_3) [8,16–22].

Mn-Al mixed oxides have not been used up to now as support for hydrodesulfurization catalysts. This is partly due to the fact manganese oxide is known to be unstable by itself. However, it can become more stable if aggregated to alumina through a sol-gel method. Fujisawa et al. [23] mentioned the importance of the oxidation state of transition metals in the catalytic activity. Mn exhibits multiple oxidation states (II, III, IV and VII) [24]. However, catalysts based on Mn (II) generally present higher catalytic activities than catalysts based on Mn (III) and Mn (IV). Manganese oxides catalysts supported on Al_2O_3 and ZrO_2 have been used as catalysts for different applications [24–26]. However, these catalysts present generally low surface areas and have the tendency to form spinels composed of Mn and Al [27]. Recently, Ho [28] reported that supported NiMnMo catalyst shows a high activity in hydrodesulfurization of sulfur compounds proving by this way that manganese is able to increase the activity of Ni-promoted $\text{MoS}_2/\text{Al}_2\text{O}_3$ catalysts.

In the present paper, NiMo catalysts supported on Mn- Al_2O_3 mixed oxide have been synthesized. The main focus of this work is to show that the addition of low percentages of manganese to alumina can help to obtain NiMoS phases with higher intrinsic activity. Catalysts characterization allows us to determine if the Ni-Mo interaction changes or remains unaffected after each stage of the catalyst preparation. Catalysts have then been characterized after each of the important steps of the preparation: drying, calcination and sulfidation.

2. Experimental

2.1. Synthesis of the Mn- Al_2O_3 supports

Mn- Al_2O_3 mixed oxides were prepared by the sol-gel method. In short, aluminum alkoxide ($\text{Al}(\text{OC}_2\text{H}_5)_3$) and manganese acetate ($\text{Mn}(\text{C}_2\text{H}_3\text{O}_2)_2$) were dissolved separately in 1-propanol (1 g alkoxide/50 mL alcohol). After homogenization, the two solutions were mixed. The gel was obtained by hydrolysis with dropwise addition of deionized water. The gel was dried at 100°C during 12 h and calcined at 500°C ($5^\circ\text{C}/\text{min}$) during 4 h. The supports with 0.1, 0.5, 1.0, 2.0 and 5.0 mol% as MnO are called AlMn0.1, AlMn0.5, AlMn1, AlMn2 and AlMn5, respectively.

2.2. Synthesis of the NiMo catalysts supported on Mn- Al_2O_3

Five series of catalysts were prepared by co-impregnation using the incipient wetness method with 14.0 wt% of MoO_3 and a $0.3 = \text{Ni}/(\text{Ni} + \text{Mo})$ molar ratio. The impregnation solution was prepared dissolving nickel nitrate hexahydrate, $\text{Ni}(\text{NO}_3)_2 \cdot 6\text{H}_2\text{O}$ and ammonium heptamolybdate tetrahydrate, $(\text{NH}_4)_6\text{Mo}_7\text{O}_{24} \cdot 4\text{H}_2\text{O}$ salts in an aqueous NH_4OH solution at pH = 9. After the impregnation step, catalysts were first dried at 120°C for 12 h before being calcined at 400°C ($5^\circ\text{C}/\text{min}$) during 4 h. The catalysts were called NiMo/AlMn $_x$ -D and NiMo/AlMn $_x$ -C where the letter x corresponds to the molar percentage of Mn as MnO on the support ($x = 0.1, 0.5, 1, 2$ and 5 mol% of MnO) and the letter D or C stands for dried or calcined catalysts, respectively.

2.3. Catalysts characterization

AlMn $_x$ supports were characterized by ζ -potential and N_2 physisorption measurements. N_2 physisorption was carried out on an ASAP 2020 Micromeritics apparatus. Samples were treated at 300°C for 4 h under vacuum at $P = 3.0 \times 10^{-5}$ mmHg before analysis. Specific surface areas and standard deviation values were determined using the ASAP 2020(v.3) software and the Brunauer-Emmet-Teller (BET) method.

ζ -potential measurements were carried out using a Malvern ZetaSizer Nano ZS90 equipment. 0.02 g of each sample was dispersed in 200 mL of a 0.01 M NaNO_3 electrolytic solution at 25°C . pH was fixed at 9 using a 0.01 M NH_4OH aqueous solution.

Catalysts at the oxide state were analyzed using UV-vis diffuse reflectance (UV-Vis DRS) and Raman spectroscopies. Raman spectra were obtained on a BWTEK i-Raman Plus spectrometer combined with a microscope (100, 50 and $20\times$), a 532 nm laser excitation source and a HQE-CCD detector. An average of 10–50 scans was obtained for each sample. The laser intensity was limited to 50 mW to avoid damage of the samples. Spectra were measured in the $1500\text{--}100\text{ cm}^{-1}$ range with a 3 cm^{-1} resolution.

UV-Vis DRS spectra were acquired on a Perkin-Elmer Lambda 35 equipment using Spectralon SRS-99-010 (99% reflectance) tablet as reference. Data are displayed using the Kubelka-Munk ($F(R_\infty)$) function:

$$F(R_\infty) = \frac{(1 - R_\infty)^2}{2R_\infty}$$

in which R_∞ is the reflectance at infinite depth. UV-Vis DRS spectra were obtained at wavelengths ranging from 200 to 1100 nm with 1 nm resolution.

Sulfided catalysts were analyzed by inductively coupled plasma optical emission spectroscopy (ICP-OES), X-ray photoelectron spectroscopy (XPS) and high resolution transmission electron microscopy (HRTEM).

Ni, Mo, and Mn amounts were determined using ICP-OES analysis on a Horiba Jobin Yvon Activa spectrometer. Before analysis,

samples were treated by a mixture of H_2SO_4 , HNO_3 , and HF (1:1:0.5, v/v/v ratio) followed by maximum evaporation.

X-Ray photoelectron spectroscopy (XPS) studies were carried out on an Axis Ultra DLD (Kratos Analytical) spectrometer using $\text{Al K}\alpha$ radiation (1486.6 eV). Sulfided samples were manipulated under Ar without contact with air and pressed on an indium foil attached to the sample holder before being inserted into the XPS instrument. Binding energies were referenced to the C 1s level of contaminating carbon at 284.6 eV.

Decomposition of the Mo 3d and Ni 2p XPS spectra were done by curve fitting line shape using mixed Gaussian and Lorentzian functions after background treatment by Shirley type baseline (CasaXPS software, version 2.0.71) [29,30]. The atomic percentage [i] of atom was determined by measuring the corresponding total peak area A_i using appropriate sensitivity factors S_i :

$$[i] = \frac{\frac{A_i}{S_i}}{\sum_{i=1}^n \left(\frac{A_i}{S_i} \right)}$$

Mo 3d and Ni 2p core level spectra can be decomposed into three contributions corresponding to MoS_2 , MoO_xS_y , MoO_3 species and to NiS_x , NiMoS , and NiO_x species respectively [31–33]. The relative amount of NiMoS phase is determined by:

$$\% \text{NiMoS} = \frac{A_{\text{NiMoS}}}{A_{\text{NiMoS}} + A_{\text{NiO}_x} + A_{\text{NiS}_x}} \times 100$$

with A_{NiMoS} , A_{NiO_x} , and A_{NiS_x} , the experimental XPS areas of respectively NiMoS , NiO_x , and NiS_x species.

HRTEM images were acquired on a JEOL 2010 (200 kV) microscope. Sulfided catalysts were ultra-sonically dispersed in ethanol. The suspension was then deposited onto a carbon-coated Cu grid. The MoS_2 -based catalysts exhibit a layered structure with particles forming more or less stacked slabs. Statistical analyses were done on 15 different micrographs (2356 nm² each one) coming from various regions of each studied sample (600–800 counted particles). Average stacking number of layers per slab and the average slab length were obtained, using the following equations [34]:

$$\bar{N} = \frac{\sum_{i=1}^n n_i N_i}{\sum_{i=1}^n n_i} \quad (3)$$

$$\bar{L} = \frac{\sum_{i=1}^n n_i l_i}{\sum_{i=1}^n n_i} \quad (4)$$

With N_i and l_i representing respectively the stacking number and the length of a MoS_2 slab as determined directly on pictures, n the number of particles measured in a size range or stacking number of index i .

2.4. Catalytic evaluation tests

Calcined catalysts were sulfided with a 4 L/h flow of 10 mol% $\text{H}_2\text{S}/\text{H}_2$ gas mixture at 400 °C (5 °C/min) for 4 h. Catalysts were labeled: $\text{NiMo}/\text{AlMn}0.1\text{-S}$, $\text{NiMo}/\text{AlMn}0.5\text{-S}$, $\text{NiMo}/\text{AlMn}1\text{-S}$, $\text{NiMo}/\text{AlMn}2\text{-S}$ and $\text{NiMo}/\text{AlMn}5\text{-S}$ respectively, where -S indicates sulfided samples.

Catalysts were evaluated in the hydrodesulfurization of a gasoline model (500 ppm S corresponding to a mixture of 0.37 M dibenzothiophene/n-heptane). Hydrodesulfurization catalytic tests were carried out in a fixed-bed micro-reactor with 0.01 g of catalyst at 30 bars. The reactor was fed with 0.3 cm³/min (STP) of liquid and 35 cm³/min (STP) of H_2 . Heptane was used as solvent because under the conditions of the HDS test ($P = 30$ bars and $T = 300$ °C), all reactants are in the gaseous phase [35].

The reaction procedure can be described as follows: the stable activity of a fresh sulfided catalyst was achieved after 12 h of reac-

tion at $T = 280$ °C with 0.12 cm³/min liquid flow. Immediately after stabilization, the liquid feed was increased to 0.3 cm³/min for 2 h. The reactor temperature was then raised to 300, 320 and 340 °C every 2 h. Liquid samples were analyzed by gas chromatography on a Perkin Elmer AutoSystem instrument with flame ionization (FID) detector and a HP Ultra 2 (30 m × 0.32 mm id.) column. Dodecane was added in the same molar amount as DBT to be used as an internal standard.

Main reaction products were biphenyl (BP) and cyclohexylbenzene (CHB).

Conversion was calculated as follows:

$$x_{\text{DBT}} = \frac{C_{\text{DBT}_0} - C_{\text{DBT}}}{C_{\text{DBT}_0}} = \frac{\sum A_i}{\sum A_i + A_{\text{DBT}}}$$

where C_{DBT_0} and C_{DBT} are the DBT molar concentration (mol L⁻¹) in the feed and at the outlet of the reactor, respectively. A_i = chromatographic areas of BP or CHB products.

Reaction rates were calculated considering a first order kinetic as follows:

$$r_{\text{DBT}} = k C_{\text{DBT}}$$

$$k = -\frac{\ln(1 - x_{\text{DBT}})}{t}$$

$$t = \frac{V C_{\text{DBT}_0}}{F_{\text{DBT}_0}}$$

$$r_{\text{DBT}_0} = -\frac{F_{\text{DBT}_0}}{m_c} \ln(1 - x_{\text{DBT}}) \quad \text{and} \quad C_{\text{DBT}} = C_{\text{DBT}_0}(1 - x_{\text{DBT}}).$$

The pseudo-first-order constant is then obtained:

$$k = -\frac{F_{\text{DBT}_0}}{m_c C_{\text{DBT}_0}} \ln(1 - x_{\text{DBT}})$$

The pseudo first order reaction is:

$$r_{\text{DBT}_0} = -\frac{F_{\text{DBT}_0}}{m_c} \ln(1 - x_{\text{DBT}})$$

where r_{DBT_0} reaction rate (mol s⁻¹ g⁻¹), k the rate constant (s⁻¹), t the space time, F_{DBT_0} the molar flow of the DBT feed (mol s⁻¹), C_{DBT_0} the molar concentration of the DBT feed (mol s⁻¹), m_c the catalyst weight (g), x_{DBT} the DBT conversion.

3. Results

3.1. Characterization of the AlMn_x supports

3.1.1. N_2 physisorption

Fig. 1 shows the N_2 adsorption-desorption isotherms of the $\text{AlMn}0.1$, $\text{AlMn}0.5$, $\text{AlMn}1$, $\text{AlMn}2$ and $\text{AlMn}5$ supports. All the AlMn_x supports present similar type IV isotherm profiles associated with the presence of a mesoporous distribution. H1 hysteresis loops are found in all cases suggesting the presence of solids consisting of particles crossed by nearly cylindrical channels or made by aggregates or agglomerates of spheroidal particles [36].

Table 1 summarizes the textural properties of the Al_2O_3 , $\text{AlMn}0.1$, $\text{AlMn}0.5$, $\text{AlMn}1$, $\text{AlMn}2$ and $\text{AlMn}5$ supports. The pore volume and average pore size values confirm the presence of a mesoporous distribution. S_{BET} specific surface areas of the $\text{AlMn}0.1$, $\text{AlMn}0.5$, $\text{AlMn}1$ and $\text{AlMn}2$ supports are relatively similar to the one found for pure alumina (366 m²/g) showing that up to 2% mol Mn as MnO , addition of manganese does not change dramatically the textural properties of alumina. However, the $\text{AlMn}5$ support exhibits a decrease in surface area to 290 m²/g. This result suggests that the alumina porosity is then covered with manganese due

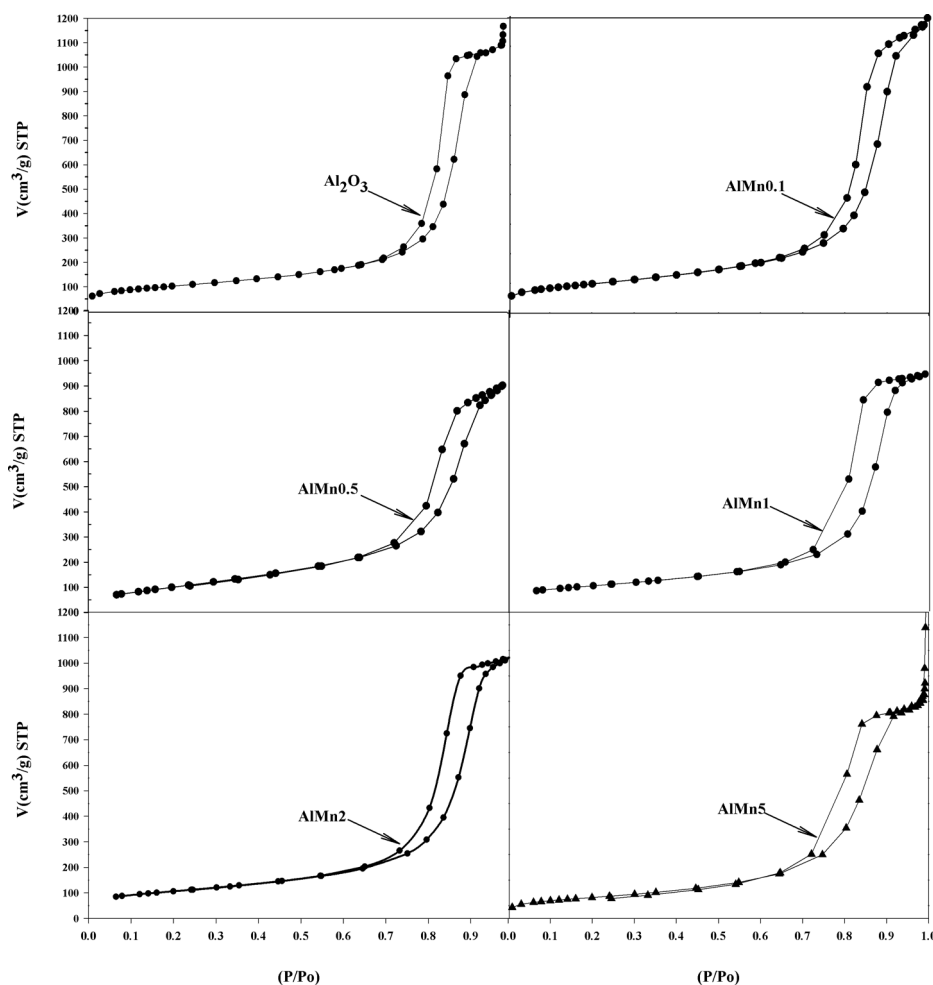


Fig. 1. N₂ adsorption-desorption isotherms of the Al₂O₃, AlMn0.1, AlMn0.5, AlMn1, AlMn2 and AlMn5 supports calcined at 500 °C.

Table 1

Textural properties of alumina, AlMn0.1, AlMn0.5, AlMn1, AlMn2 and AlMn5 supports.

Support	Specific surface area (m ² /g)	Porous volume (cm ³ /g)	Average pore size (nm)
Al ₂ O ₃	366 ± 1	1.7	18.4
AlMn0.1	354 ± 1	1.5	16.8
AlMn0.5	379 ± 5	1.4	14.6
AlMn1	363 ± 1	1.5	16.2
AlMn2	380 ± 1	1.5	16.6
AlMn5	290 ± 2	1.4	19.6

Table 2

Net surface pH values of the Al₂O₃, AlMn0.1, AlMn0.5, AlMn1, AlMn2 and AlMn5 supports.

Support	Net surface pH
Al ₂ O ₃	8.6
AlMn0.1	8.6
AlMn0.5	8.5
AlMn1	8.2
AlMn2	7.8
AlMn5	7.1

to the higher manganese concentration on the support. However, porous volume remains relatively constant whatever the amount of manganese. Average pore size values first decrease from 18.4 to 16.8 and 14.6 nm when adding 0.1 and 0.5 mol% Mn, respectively before increasing again to 16.2, 16.6 and 19.6 nm when 1.0, 2.0 and 5.0 mol% Mn are respectively used. These results suggest that an initial preferential blocking of the smallest alumina pores occurred when the supports have a low manganese concentration. In the case of the AlMn5 support, the creation of a certain porosity is observed resulting from the covering of Al₂O₃ by manganese species.

3.1.2. ζ -potential measurements

Fig. 2 shows the ζ potential curves of the different supports. In the pH = 1–7 range, the ζ -potential tends to decrease slightly with Mn addition up to AlMn1 but more rapidly for the supports with a higher manganese concentration (AlMn2 and AlMn5). In the

pH = 8–12 range, the ζ -potential values become negative whatever the Mn concentration.

Point-of-zero charge values, obtained from the intersection of the ζ -potential curve with the pH axis, can be associated with the net surface pH of the oxide [37]. The point of zero charge (PZC) or net surface pH of the alumina is reported between 7.5 and 9.0 suggesting a slight basic character [38]. Table 2 reports the net surface pH of the alumina, AlMn0.1, AlMn0.5, AlMn1, AlMn2 and AlMn5 obtained from Fig. 2.

Up to AlMn0.5, the Mn-containing supports have similar net surface pH values to the alumina (pH = 8.6). However, above 1 mol% Mn as MnO, net surface pH values of the mixed oxides decrease significantly when increasing the amount of Mn reaching a value of 7.1 for AlMn5. These results suggest a modification of the surface charge of the alumina due to the presence of Mn. Therefore, PZCs are shifted to lower values as expected when adding an acid component like manganese oxides [26].

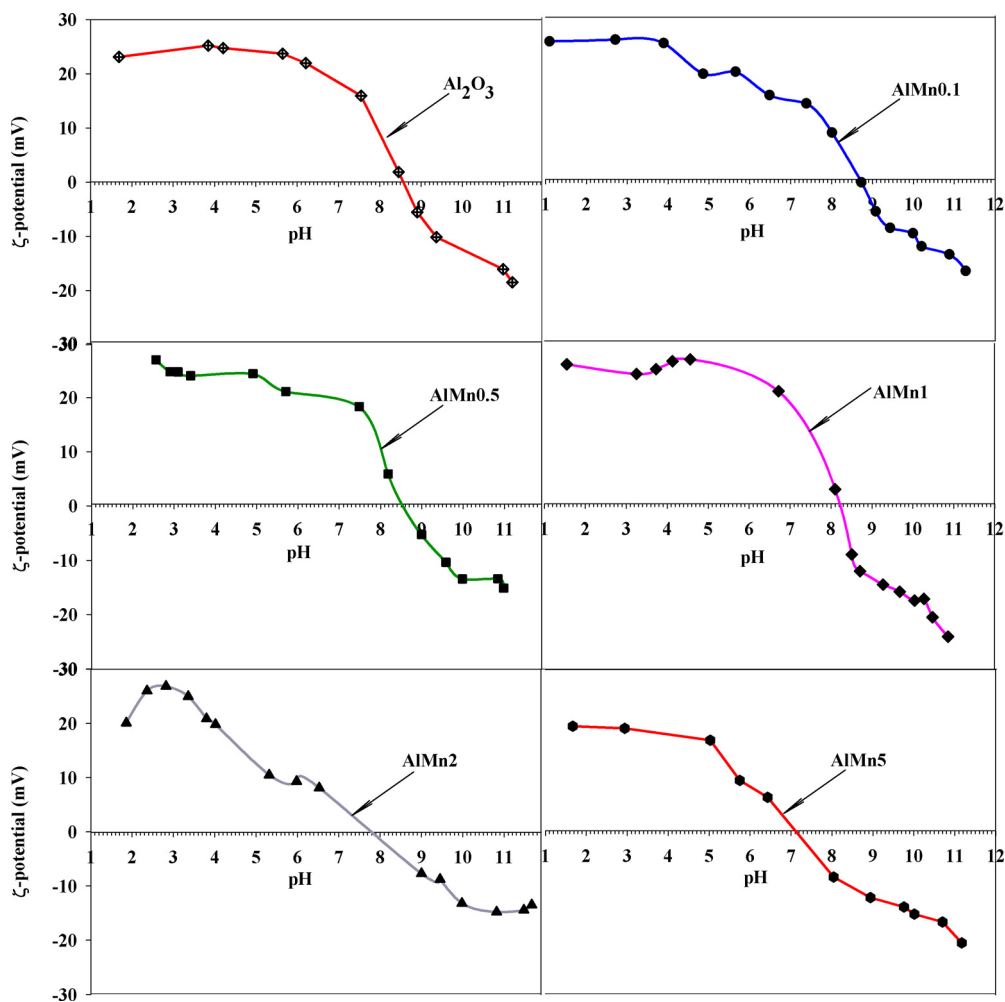


Fig. 2. ζ -potential curves of the Al_2O_3 , AlMn0.1 , AlMn0.5 , AlMn1 , AlMn2 and AlMn5 supports calcined at 500°C .

Table 3
Charge-transfer and d-d transition bands of manganese species.

Compound	Mn^{n+}	λ (nm)	Assignment
MnO	Mn^{2+}	420	${}^6\text{A}_{1g} \rightarrow {}^4\text{A}_{1g}$
		500	${}^6\text{A}_{1g} \rightarrow {}^4\text{T}_{2g}$
		610	${}^6\text{A}_{1g} \rightarrow {}^4\text{T}_{2g}$
Mn_3O_4	Mn^{2+}	255	$\text{O}^{2-} \rightarrow \text{Mn}^{2+}$
	Mn^{3+}	320	$\text{O}^{2-} \rightarrow \text{Mn}^{3+}$
Mn_2O_3	Mn^{3+}	370	${}^5\text{B}_{1g} \rightarrow {}^5\text{B}_{2g}$
		485	${}^5\text{B}_{1g} \rightarrow {}^5\text{E}_g$
		755	${}^5\text{B}_{1g} \rightarrow {}^5\text{A}_{1g}$
		755	${}^5\text{B}_{1g} \rightarrow {}^5\text{A}_{1g}$
Mn- Al_2O_3	Mn^{2+}	422	${}^6\text{A}_{1g} \rightarrow {}^4\text{A}_{1g}$
	Mn^{3+}	485	${}^5\text{E}_g \rightarrow {}^5\text{T}_{2g}$
	Mn^{4+}	470	${}^4\text{A}_{2g} \rightarrow {}^4\text{T}_{2g}$

3.1.3. UV–Vis diffuse reflectance (UV–Vis DRS) spectroscopy

Manganese oxide can exhibit different oxidation states, the most common being Mn^{2+} , Mn^{3+} , or Mn^{4+} [39]. Velú et al. [24] reported diffuse reflectance UV–Vis spectra of Mn references with different oxidation states. Bands reported from UV–Vis reflectance spectroscopy studies of manganese species are summarized in Table 3.

AlMn0.1 , AlMn0.5 , AlMn1 , AlMn2 and AlMn5 supports were studied after calcination step at 500°C (Fig. 3). For comparison purposes, the spectra of pure alumina is also reported. The much higher intensity of the bands observed on Mn-containing solids shows that UV–vis DRS profiles are dominated by contributions coming from manganese. In the 200–380 nm range, all AlMn_x supports show a band at 255 nm associated with an $\text{O}^{2-} \rightarrow \text{Mn}^{2+}$ charge transfer

as well as a shoulder at 320 nm associated with the $\text{O}^{2-} \rightarrow \text{Mn}^{3+}$ process. The 255 nm band shows an increased intensity when increasing the Mn content to 5 mol%. Moreover, by comparison to the 255 nm band, the relative contribution of the shoulder at 320 nm remains constant up to AlMn1 showing that the proportion of manganese as Mn^{3+} stays unchanged up to 2 mol%. However, increasing further the Mn concentration as in AlMn5 leads to a strong increase of the 320 nm signal showing a higher Mn^{3+} proportion in this latter case. In the 400–700 nm range, AlMn0.1 , AlMn0.5 , AlMn1 and AlMn2 supports show a band at 470 nm due to Mn^{4+} (Fig. 3). This latter band indicates that Mn^{2+} , initially present in the manganese acetate precursor, is oxidized to Mn^{3+} but also to Mn^{4+} after calcination. For the AlMn5 support, this band shifts to 485 nm showing in this case Mn^{3+} species in interaction with Al_2O_3 (Table 3).

3.2. Catalysts characterization at the oxide state

3.2.1. UV–Vis diffuse reflectance spectra of the Ni/ AlMn5 reference catalyst

During the preparation of the $\text{NiMo}/\text{AlMn}_x$ catalysts, it is essential to differentiate Ni–Mo interactions from Ni-only-support interactions. For this purpose, a Ni catalyst supported on AlMn5 catalyst was prepared using an impregnation solution at pH = 9. Catalyst was calcined at the same temperature as for the $\text{NiMo}/\text{AlMn}_x$ catalysts (400°C). Figure S1 (Supplementary Information) shows the UV–Vis diffuse reflectance spectra of AlMn5 and of $\text{Ni}/\text{AlMn5}$ –

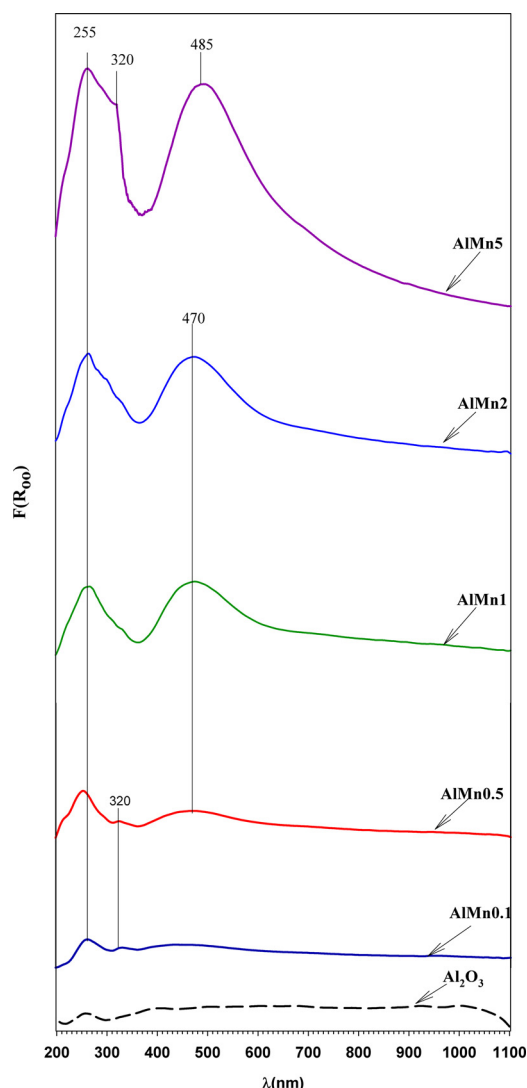


Fig. 3. UV-Vis diffuse reflectance spectra of alumina, AlMn0.1, AlMn0.5, AlMn1, AlMn2 and AlMn5 supports, calcined at 500 °C.

C. Similarly to AlMn5, the Ni/AlMn5-C solid shows bands at 255, 320 and 485 nm which are characteristics of Mn^{2+} (255 nm) and of Mn^{3+} (320 and 485 nm). Also, a clear contribution at 380 nm (absent on the support only) is observed and corresponds to the formation of the NiMnO spinel. In this spinel compound, Ni^{2+} strongly interacts with Mn(III) species from the support. This suggests that Ni tends to interact with the support when the manganese concentration is high.

3.2.2. Characterization of the NiMo catalysts supported on AlMn0.1

3.2.2.1. UV-Vis diffuse reflectance spectroscopy analysis. Fig. 4 shows the UV-Vis diffuse reflectance spectra of the NiMo catalysts supported on AlMn0.1 after drying at 120 °C and after calcination at 400 °C. Bands associated with charge transfer processes due to Mo (255–320 nm) strongly overlap with the Mn^{2+} band at 255 nm. However, the much higher intensity of NiMo/AlMn0.1 compared to the AlMn0.1 support alone suggests that in the present case, the charge transfer bands in the 200–350 nm range are directly related to the state of Mo oxides. Comparison between the AlMn0.1 support and the NiMo/AlMn0.1-D catalyst spectra also allows showing that the deposition of Ni/Mo species on the AlMn0.1 support generates two contributions at 257 and 300 nm corresponding respectively

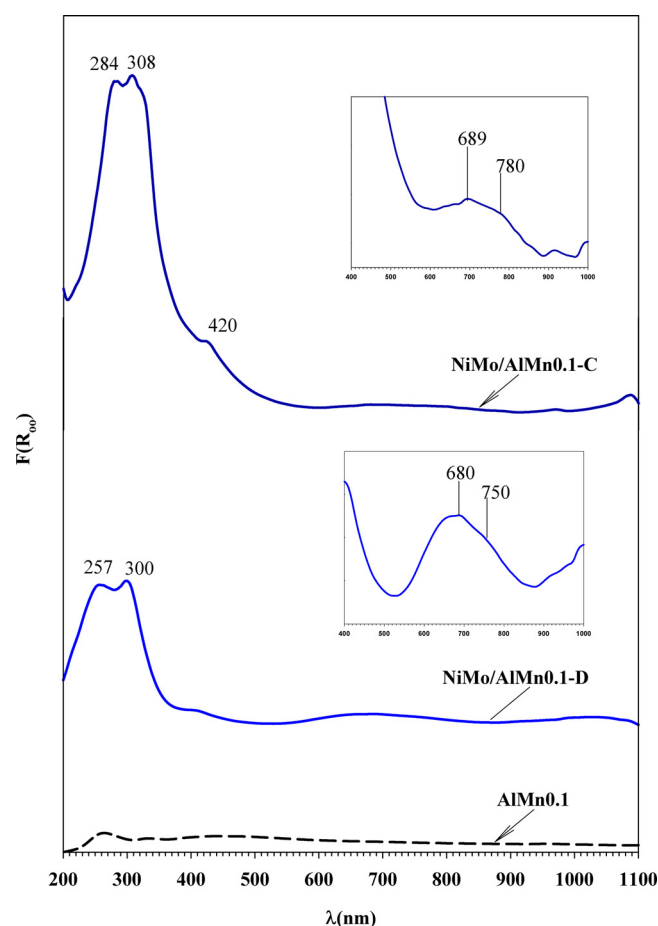


Fig. 4. UV-Vis diffuse reflectance spectra of the NiMo catalysts supported on AlMn0.1, after drying at 120 °C (-D) and after calcination at 400 °C (-C).

to tetrahedral and octahedral molybdenum oxides [40]. Their relative similar intensities suggest roughly a similar proportion of tetrahedral and octahedral species. Mn^{2+} species as in Mn_3O_4 is expected to give rise to a contribution also at 255 nm. However, this band must be accompanied by a Mn^{3+} contribution around 320 nm (Table 3) absent here. Therefore, the 257 nm band here can be safely attributed only to Mo oxide species. Moreover, a shoulder at 420 nm corresponding to the ${}^6\text{A}_{1g} \rightarrow {}^4\text{A}_{1g}$ transition of Mn^{2+} in interaction with Al_2O_3 can also be detected. The calcination leads to a strong increase of the bands between 200 and 500 nm but also to a shift of the charge transfer bands due to Mo to higher wavelength (284 and 308 nm respectively). This shift indicates that calcination leads to the transformation of the tetrahedral molybdenum oxide species into octahedral ones. Therefore, these results suggest that the NiMo catalyst supported on AlMn0.1 presents only the Mn(II) oxidation state while octahedral molybdenum oxide species predominate after calcination. Moreover, the NiMo/AlMn0.1-D catalyst shows two bands at 680 and 750 nm which are related to the nickel ion with octahedral and distorted-octahedral local symmetries, $\text{Ni}^{2+}(\text{Oh})$ and $\text{Ni}^{2+}(\text{Oh}_{\text{dis}})$, respectively. These bands shift to higher wavelength after calcination particularly for distorted-octahedral Ni showing some changes of the local environment leading to an even more distorted symmetry.

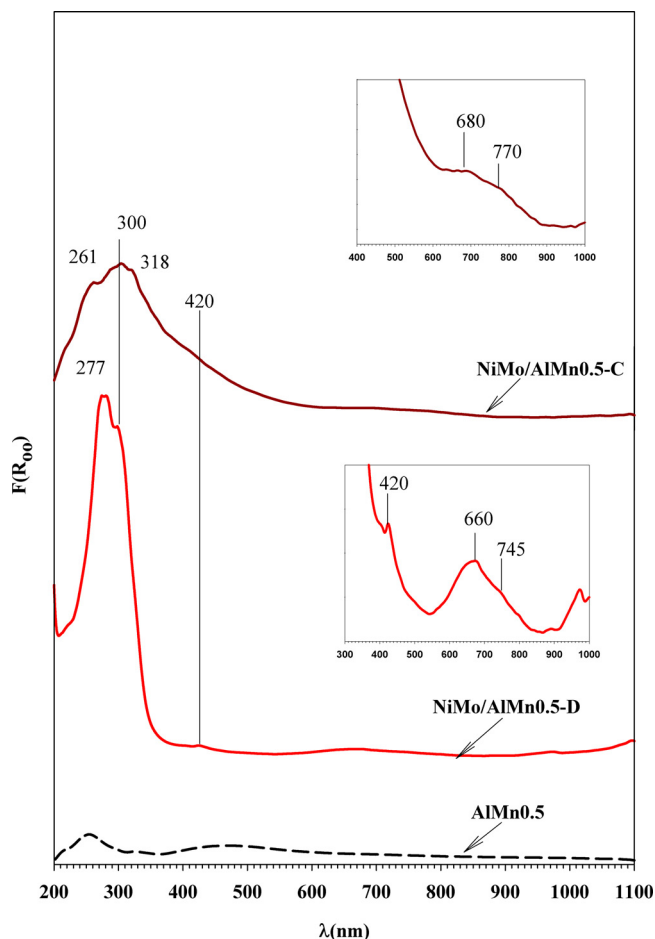


Fig. 5. UV-Vis diffuse reflectance spectra of NiMo catalysts supported on AlMn0.5, dried at 120 °C (-D) and calcined at 400 °C (-C).

3.2.2.2. Raman spectroscopy analysis. Mo species present on NiMo/AlMn0.1-D and NiMo/AlMn0.1-C catalysts were analyzed by Raman spectroscopy (Figure S2). The presence of some fluorescence due to manganese incorporated to the alumina support tends however to lower the signal to noise ratio complicating the work of attribution of bands. The Raman spectrum of NiMo/AlMn0.1-D shows a weak band at 930 cm^{-1} characteristic of MoO_4^{2-} in agreement with the fact these species are favored when the impregnating step is performed at pH=9. Moreover, the calcination procedure does not modify the Raman response.

These results suggest that the MoO_4^{2-} species initially present in solution remain mainly unchanged after the impregnation and calcination steps. Therefore, MoO_4^{2-} species would be here in interaction with Ni^{2+} entities.

3.2.3. Characterization of NiMo catalysts supported on AlMn0.5

3.2.3.1. UV-Vis diffuse reflectance spectroscopy analysis. Fig. 5 shows the UV-Vis diffuse reflectance spectra of NiMo catalysts supported on AlMn0.5, dried at 120 °C and calcined at 400 °C. In the case of NiMo/AlMn0.5-D, strong intense charge transfer bands are observed at 277 nm and 300 nm. Since, the band at 255 nm due to $\text{O}^{2-} \rightarrow \text{Mn}^{2+}$ charge transfer is quite weak as observed on AlMn0.5, the two bands can be safely attributed mainly to octahedral Mo oxide species. A signal at 420 nm once again reveals the presence of Mn^{2+} species. This result shows a higher proportion of octahedral and more polymerized Mo species at the dried state when increasing the Mn content from 0.1 mol% to 0.5 mol% showing an influence of manganese on the state of Mo oxide species. After cal-

cination, the UV-vis curve shows a lower but broader profile in the 200–500 nm range showing a higher heterogeneity in terms of Mo oxide species while a clear shoulder at 261 nm due to Mn^{2+} can now be observed as expected in Mn_3O_4 . In this case, a Mn^{3+} contribution would also be expected around 320 nm (Table 3) which might explain the shoulder observed at 318 nm. Similarly, the shoulder at 420 nm due to Mn^{2+} in interaction with Al_2O_3 is also observed. These results clearly identify a higher contribution of Mn signals in the UV-vis profile after calcination suggesting some migration of manganese oxide species to the surface of the Mn- Al_2O_3 support.

About Ni species, at the dried state, two bands at 660 and 745 nm due respectively to octahedral and distorted-octahedral Ni can still be observed. These bands shift once again to higher wavelength after calcination showing a more distorted environment in this case.

3.2.3.2. Raman spectroscopy analysis. The NiMo/AlMn0.5-D shows a wide band with a maximum at 940 cm^{-1} characteristic of $\text{Mo}_7\text{O}_{24}^{6-}$ species [41] (Figure S3) suggesting the formation of more polymerized Mo oxide species after the impregnation step in this case in agreement with UV-vis results. This band however presents a significant tail to lower wavelength showing also the presence of MoO_4^{2-} species. A band at 1044 cm^{-1} is also observed but is characteristic of nitrate ion species coming from the nickel nitrate salt. After calcination, the main band due to $\text{Mo}_7\text{O}_{24}^{6-}$ species is still observed with a maximum at 940 cm^{-1} . However, this band appears broader in agreement with a higher heterogeneity of Mo oxide species as also observed by UV-vis DRS. Moreover, this band tends to extend to higher shift values showing a higher proportion of polymerized species than after the drying step.

3.2.4. Characterization of the NiMo catalysts supported on AlMn1

3.2.4.1. UV-Vis diffuse reflectance spectroscopy analysis. Fig. 6 shows the UV-Vis diffuse reflectance spectra of NiMo/AlMn1-D and NiMo/AlMn1-C catalysts. In the case of the dried NiMo/AlMn1-D solid, charge transfer bands due to Mo are observed at 288 and 310 nm showing the formation of octahedral Mo oxide species. Interestingly, a progressive shift to higher wavelength of these charge transfer bands can be noticed when increasing the Mn content from 257 nm with 0.1% Mn to 277 nm with 0.5% Mn and finally here 288 nm with 1.0% Mn. This suggests the formation of more and more Mo oxide species with a higher degree of polymerization when increasing the Mn content. Manganese transition bands can also be detected at 420 and 470 nm due to Mn^{2+} and Mn^{4+} species in interaction with Al_2O_3 respectively.

After calcination, the charge transfer bands region becomes more complex with a tail extending up to 600 nm. On the calcined solid, the contributions due to transition bands of Mn^{2+} and Mn^{4+} species are much more significant. This shows clearly that the calcination step results in an enrichment in manganese at the solid surface. In this respect, a clear shoulder at 267 nm due to the $\text{O}^{2-} \rightarrow \text{Mn}^{2+}$ charge transfer band is observed while the contribution due to the $\text{O}^{2-} \rightarrow \text{Mn}^{3+}$ charge transfer band around 330 nm also shows the presence of some Mn^{3+} species. Moreover, the shoulder at 390 nm could result from the ${}^5\text{B}_{1g} \rightarrow {}^5\text{B}_{2g}$ transition band of Mn^{3+} . Finally, the tail extending to 600 nm suggests other undefined contributions due to Mn^{2+} or Mn^{4+} species.

About nickel species, the bands initially present at 640 and 750 nm and due to octahedral and distorted-octahedral species shift to 680 and 780 nm after calcination in a similar way as for previous cases.

3.2.4.2. Raman spectroscopy analysis. Fig. 7 shows the Raman spectra of NiMo catalysts supported on AlMn1. The NiMo/AlMn1-D solid shows a band at 1044 cm^{-1} characteristic of nitrate species and a wide band with a maximum at 945 cm^{-1} related to $\text{Mo}_7\text{O}_{24}^{6-}$

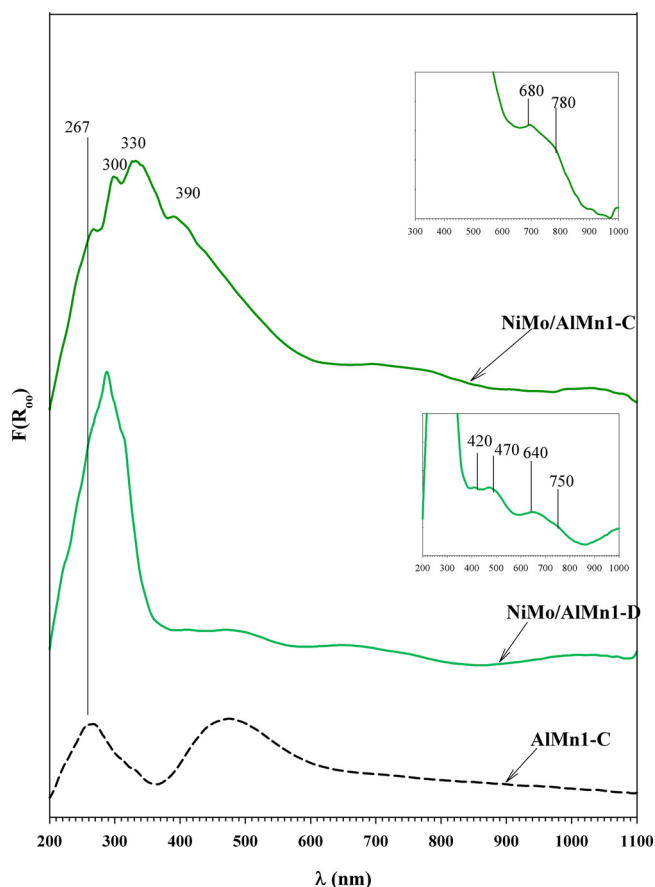


Fig. 6. UV-Vis diffuse reflectance spectra of NiMo catalysts supported on AlMn1, dried at 120 °C (-D) and calcined at 400 °C (-C).

species. Calcination once again does not have any influence on the position of this latter vibration band. However, compared to the AlMn0.5 case, a slight shift of 5 cm^{-1} to higher wavenumbers is observed here suggesting in agreement with previous UV-vis results a slightly higher polymerization degree in the present case.

3.2.5. Characterization of the NiMo catalysts supported on AlMn2

3.2.5.1. UV-vis diffuse reflectance spectroscopy analysis. Fig. 8 shows the UV-Vis diffuse reflectance spectra of NiMo/AlMn2-D and NiMo/AlMn2-C catalysts. The NiMo/AlMn2-D solid presents charge transfer bands due to Mo with maximum at 288 nm showing no more shift to higher wavelength when increasing the Mn content to 2.0 mol%. However, the shoulder around 310–315 nm appears here slightly more intense than for NiMo/AlMn1-D. The Mn^{2+} contribution characterized by a shoulder at 265 nm and corresponding to the $\text{O}^{2-} \rightarrow \text{Mn}^{2+}$ charge transfer is still observed while the large band centered at 470 nm and due to Mn^{4+} species is now more clearly defined. It should also be noted that the weak transition band due to Mn^{2+} at 420 nm cannot be really detected anymore. Finally, a weak signal corresponding to the formation of a NiMnO spinel phase can now be detected at 380 nm.

After calcination, the UV-vis profile is once again more complex with maximum at 288 nm but with shoulders more clearly detectable at 315, 330, and even 380 nm. The contribution at 315 nm suggests the presence of Mo oxide species with quite high polymerization degree. As observed before, the shoulder at 330 nm corresponds to Mn^{3+} species showing probably some oxidation of Mn^{2+} species into Mn^{3+} during calcination. This higher formation of Mn^{3+} species also leads to a more discernible shoulder at 380 nm due to the NiMnO spinel phase and resulting from the reac-

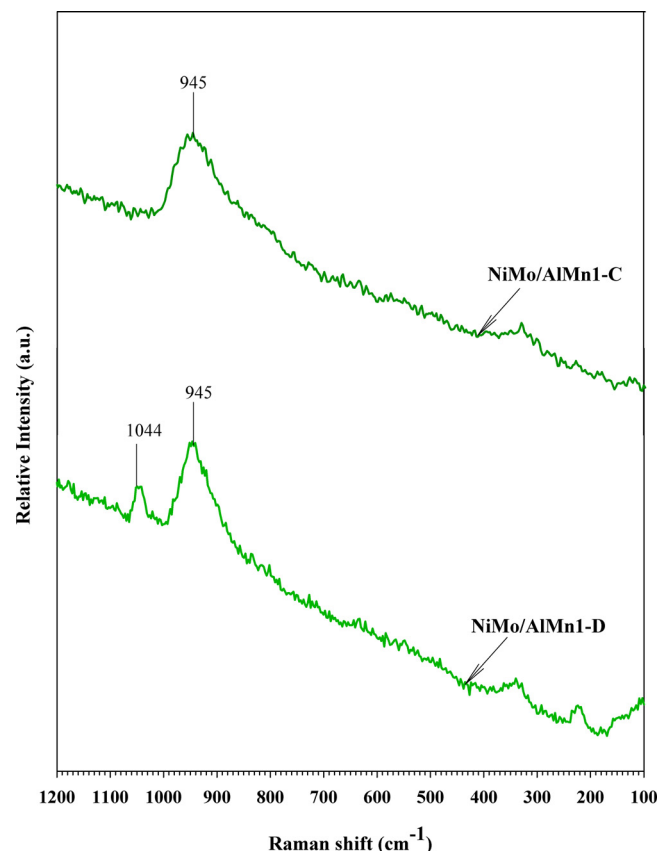


Fig. 7. Raman spectra of NiMo catalysts supported on AlMn1, dried at 120 °C (-D) and calcined at 400 °C (-C).

tion between Mn^{3+} and Ni^{2+} species. Finally, the tail extending to 600 nm results from the Mn^{4+} contribution which appears stronger suggesting an ever high tendency for manganese to migrate to the solid surface after calcination.

Similar nickel contributions to previous cases and due to octahedral and distorted octahedral species can still be observed on the dried samples. These bands shift to higher wavelength after calcination.

3.2.5.2. Raman spectroscopy analysis. Figure S4 shows the Raman spectra of NiMo/AlMn2-D and NiMo/AlMn2-C solids. After both drying and calcination, a very large band going from 910 to 980 cm^{-1} is observed with a maximum at this latter value corresponding to $\text{Mo}_8\text{O}_{26}^{4-}$ species. The large bandwidth also suggests contributions coming from MoO_4^{2-} and $\text{Mo}_7\text{O}_{24}^{6-}$ species. Therefore, a further polymerization of Mo oxide species is confirmed for the AlMn2-supported NiMo case.

3.2.6. Characterization of the NiMo catalysts supported on AlMn5

3.2.6.1. UV-vis diffuse reflectance spectroscopy analysis. Fig. 9 shows the UV-vis diffuse reflectance spectra of NiMo/AlMn5-D and NiMo/AlMn5-C catalysts. The increase of the manganese concentration to 5 mol% as MnO leads to a complete change of the UV-vis profile on the dried solid showing only the signature expected from manganese contributions (see for comparison, the UV-vis curve of the AlMn5 support alone). Indeed, two main charge transfer bands observed at 255 and 320 nm are ascribed to Mn^{2+} and Mn^{3+} species. Moreover, the large band at higher wavelength now shifts to 485 nm confirming a higher proportion of Mn^{3+} species in this case (Table 3). Through interaction with Ni^{2+} species, this high Mn^{3+}

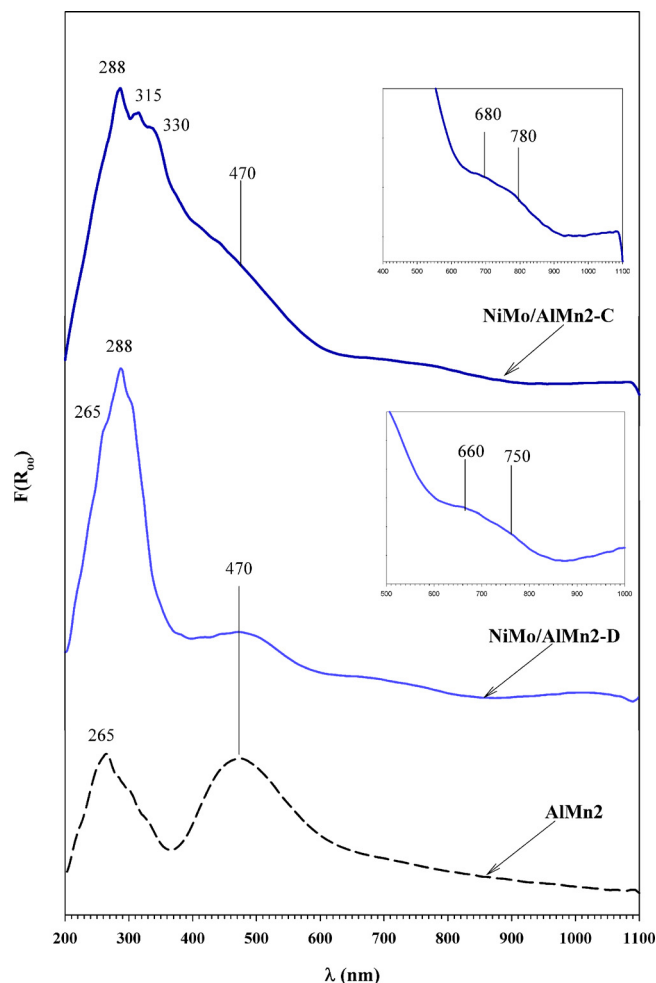


Fig. 8. UV-Vis diffuse reflectance spectra of NiMo catalysts supported on AlMn₂, dried at 120 °C (-D) and calcined at 400 °C (-C).

amount favors the formation of NiMnO spinel as confirmed by the presence of a band at 380 nm.

After calcination, the contribution at 320 nm becomes more intense than the one at 255 nm showing that calcination induces the oxidation of some Mn²⁺ species into Mn³⁺. Similarly, the large band at 485 nm appears more intense. This higher amount of Mn³⁺ species leads as expected to more NiMnO moieties as confirmed by the better defined contribution at 380 nm.

3.2.6.2. Raman spectroscopy analysis. Figure S5 shows the Raman spectra of NiMo/AlMn5-D and NiMo/AlMn5-C catalysts. The NiMo/AlMn5-D solid shows a band at 930 cm⁻¹ related to MoO₄²⁻. After calcination, the NiMo/AlMn5-C shows a wider band going this time from 910 to 950 cm⁻¹ with a maximum at 930 cm⁻¹ corresponding to MoO₄²⁻ and Mo₇O₂₄⁶⁻ species. More importantly, a band at 990 cm⁻¹ due to MoO₃ clusters is now observed showing a strong negative impact of a high manganese concentration on the Mo oxide dispersion.

3.2.7. Characterization summary of the NiMo/AlMn_x catalysts at the oxide state

A summary of the results about Mn and Mo species for the series of catalysts supported on AlMn_{0.1}, AlMn_{0.5}, AlMn₁, AlMn₂, and AlMn₅ using UV-DRS and Raman spectroscopies is shown in Table 4. The manganese concentration of the AlMn_x supports clearly influences the degree of Mn oxidation as well as the nature of the Mo oxide species formed. About Mn oxidation state, while

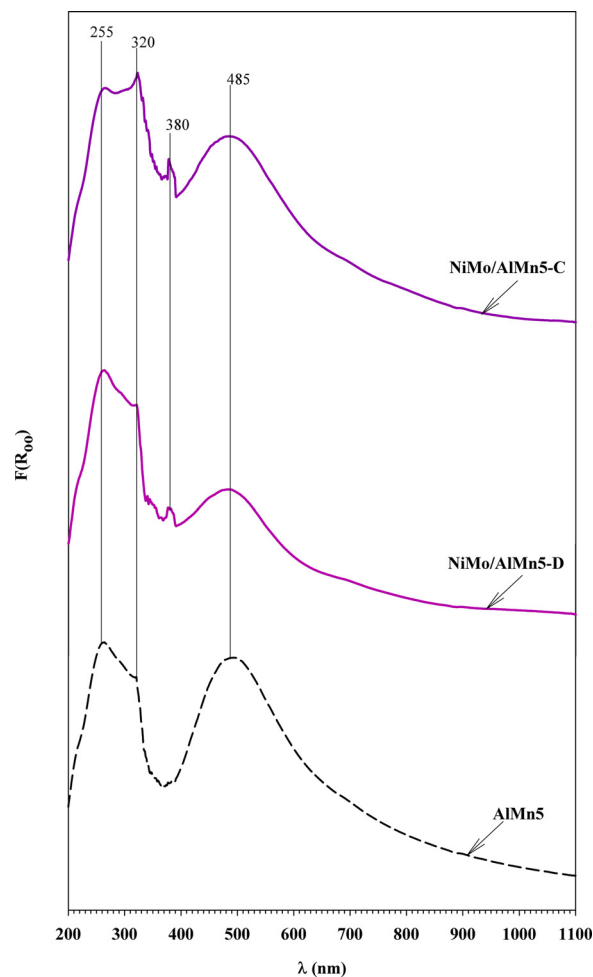


Fig. 9. UV-Vis diffuse reflectance spectra of NiMo catalysts supported on AlMn₅, dried at 120 °C (-D) and calcined at 400 °C (-C).

Table 4

Summary of the Mn and main Mo species formed on AlMn_x supports (0.1 ≤ x ≤ 5.0) after drying and calcination steps as characterized by Raman and DRS-UV-Vis spectroscopies.

Catalyst	Impregnation at pH = 9	
	Dried	Calcined
NiMo/AlMn0.1	Mn ²⁺ -Al ₂ O ₃ MoO ₄ ²⁻	Mn ²⁺ -Al ₂ O ₃ MoO ₄ ²⁻
NiMo/AlMn0.5	Mn ²⁺ -Al ₂ O ₃	Mn ²⁺ -Al ₂ O ₃ > Mn ³⁺ -Al ₂ O ₃ Mn ²⁺ and Mn ³⁺ (as in Mn ₃ O ₄)
NiMo/AlMn1	Mo ₇ O ₂₄ ⁶⁻ Mn ²⁺ -Al ₂ O ₃ ≅ Mn ⁴⁺ -Al ₂ O ₃ Mn ²⁺ and Mn ³⁺ (as in Mn ₃ O ₄)	Mo ₇ O ₂₄ ⁶⁻ Mn ²⁺ -Al ₂ O ₃ ≅ Mn ⁴⁺ -Al ₂ O ₃ Mn ²⁺ and Mn ³⁺ (as in Mn ₃ O ₄) Mn ³⁺ (as in Mn ₂ O ₃)
NiMo/AlMn2	Mo ₇ O ₂₄ ⁶⁻ Mn ⁴⁺ -Al ₂ O ₃ Mn ²⁺ and Mn ³⁺ (as in Mn ₃ O ₄) NiMnO	Mo ₇ O ₂₄ ⁶⁻ Mn ⁴⁺ -Al ₂ O ₃ Mn ²⁺ and Mn ³⁺ (as in Mn ₃ O ₄) Mn ³⁺ (as in Mn ₂ O ₃) NiMnO
NiMo/AlMn5	Mo ₈ O ₂₆ ⁴⁻ Mn ³⁺ -Al ₂ O ₃ Mn ²⁺ and Mn ³⁺ (as in Mn ₃ O ₄) NiMnO MoO ₄ ²⁻	Mo ₈ O ₂₆ ⁴⁻ Mn ³⁺ -Al ₂ O ₃ Mn ²⁺ and Mn ³⁺ (as in Mn ₃ O ₄) NiMnO MoO ₄ ²⁻ , Mo ₇ O ₂₄ ⁶⁻ , MoO ₃

at low Mn concentration (NiMo/AlMn0.1 and NiMo/AlMn0.5 cases), Mn²⁺ species in interaction with Al₂O₃ predominates, at higher Mn concentration (NiMo/AlMn1 and NiMo/AlMn2 cases), manganese also exists as Mn⁴⁺ in interaction with Al₂O₃ and as Mn²⁺ and Mn³⁺

Table 5

Ni, Mo, Mn, and S amounts determined by ICP-OES and/or XPS for the NiMo/Al₂O₃-S reference and the NiMo/AlMn_x catalysts with x = 0.1, 0.5, 1.0, and 2.0. Ni/(Ni + Mo) atomic ratios are also given using both techniques while S/(Ni + Mo) atomic ratio are determined using XPS data only.

Catalysts	ICP-OES				XPS					
	Mo (wt%)	Ni (wt%)	Mn (wt%)	Ni/(Ni + Mo) atomic ratio	Mo (wt%)	Ni (wt%)	S (wt%)	Mn (wt%)	S/(Ni + Mo) atomic ratio	Ni/(Ni + Mo) atomic ratio
NiMo/Al ₂ O ₃ -S	8.39	2.32	–	0.31	8.5	2.3	5.2	–	1.27	0.30
NiMo/AlMn0.1-S	8.60	2.30	0.03	0.30	8.4	2.0	5.3	–	1.36	0.27
NiMo/AlMn0.5-S	8.28	2.23	0.11	0.31	9.5	2.2	5.4	–	1.24	0.28
NiMo/AlMn1-S	7.88	2.14	0.32	0.31	8.1	2.0	5.9	0.2	1.56	0.28
NiMo/AlMn2-S	8.10	2.25	1.95	0.31	8.4	1.9	5.7	0.2	1.49	0.28

species but without direct interaction with Al₂O₃. Increasing further the Mn concentration as in the NiMo/AlMn5 case leads to a complete modification with mainly Mn³⁺ species directly interacting with Al₂O₃. Moreover, the calcination treatment leads to an enhancement of the Mn signature on UV–vis profiles suggesting that calcining AlMn_x supports induces migration of manganese to the solid surface. This also leads to the oxidation of some Mn²⁺ species to Mn³⁺.

The Mn oxidation state also directly influences the degree of polymerization of Mo oxide species. Mn(II) with its d⁵ electronic configuration, presents poor reducing ability [23] and cannot interact strongly with Ni and Mo species. This favors the formation of higher polymerized Mo oxide species as soon as the AlMn0.5 case. Mn(IV) is known to be a poor reductant but a strong oxidant and is rarely stable. Its intermediate predominant formation is only found in the NiMo/AlMn2 case. Its presence further favors polymerization of Mo oxide species. On the AlMn5 support, manganese tends to mainly cover the surface of Mo oxide species while Mn(III) in interaction with Al₂O₃ now predominates acting both as reductant and oxidant. Ni surface species can therefore react with Mn(III) leading to the formation of the NiMnO spinel phase and limiting the interaction of Ni with Mo oxide species. This lower Ni/Mo interaction also hampers the dispersion of Mo oxide entities leading to the appearance of MoO₃ clusters after calcination.

3.3. Catalyst characterization at the sulfide state

3.3.1. ICP-OES and X-ray photoelectron spectroscopy (XPS) analyses of the NiMo sulfide catalysts

As observed in the previous section, Mn can strongly influence the nature of the Mo oxide species formed after drying and calcination steps. This also suggests that the addition of manganese could also modify after sulfidation the dispersion of the active phase as well as the amount of Ni-promoted MoS₂. To verify this hypothesis, sulfided catalysts were first analyzed by ICP-OES and XPS.

Ni, Mo, and Mn contents were determined using both elemental analysis and X-ray photoelectron spectroscopy. The different amounts are reported in Table 5. Results show a good agreement between theoretical and experimental values. XPS and ICP-OES results of Mo and Ni contents are similar for all catalyst series showing a good homogeneity in dispersion of the Ni/MoS₂ particles without any particular surface enrichment in Ni or Mo. In the case of Mn, ICP-OES results differ from those acquired using XPS. Indeed, using XPS, Mn is not detected up to 0.5 mol% Mn (as MnO). For NiMo/AlMn1-S and NiMo/AlMn2-S, Mn is detected again by XPS but at an atomic concentration lower than using ICP-OES measurements.

Moreover, it should be noted that the persistence of a Mn signal observed by XPS after sulfidation coincides with strong contributions from Mn species in interaction with Al₂O₃ as shown in Figs. 6 and 8 for Mn contents of 1.0 mol% or higher. This shows that Mn species interacting with Al₂O₃ are strongly stabilized during the sulfidation procedure, they remain on the support surface

Table 6

Respective proportions of the different Mo and Ni species obtained from decomposition of Mo 3d and Ni 2p core level spectra.

Catalyst	Mo 3d (%)			Ni 2p (%)		
	MoS ₂	MoO _x S _y	MoO _x	NiS _x	NiMoS	NiO _x
NiMo/Al ₂ O ₃ -S	76.0	9.0	15.0	28.9	56.2	14.9
NiMo/AlMn0.1-S	62.5	17.1	20.4	35.7	44.6	19.7
NiMo/AlMn0.5-S	59.5	31.9	8.6	27.1	55.0	17.9
NiMo/AlMn1-S	74.0	11.2	14.8	31.7	50.3	18.0
NiMo/AlMn2-S	67.7	16.4	15.9	44.7	39.8	15.5

and are able to interact with the active phase (vide infra). On the opposite, bulk Mn oxide species without support interaction are not detectable anymore after sulfidation.

However, it should also be noted that the reappearance of some Mn at the catalyst surface also results in a better sulfidation of the respective catalysts particularly if one compares the S/(Ni + Mo) atomic ratios (1.49–1.56) with the value obtained for the NiMo/Al₂O₃-S reference (1.27). Finally, Ni/(Ni + Mo) atomic ratios are close to the optimal value of 0.3 using both ICP-OES and XPS.

Table 6 shows the results obtained from the decomposition of Mo 3d and Ni 2p core level spectra. The Mo 3d spectra decomposition procedure has been reported previously [32,33,42,13]. The Mo 3d spectral region contains Mo 3d_{5/2} and Mo 3d_{3/2} contributions. Three Mo 3d doublets are found as follows: (1) a Mo 3d_{5/2} and Mo 3d_{3/2} doublet with binding energies respectively at 229.0 and 232.0 eV associated with Mo⁴⁺ species of the MoS₂ phase, (2) a doublet with binding energies at 230.0 and 233.4 eV correlated with Mo⁵⁺ species of a MoO_xS_y oxysulfide phase, and (3) finally, the doublet with binding energies at 232.1 and 235.3 eV related to Mo⁶⁺ oxide species. In addition, this spectral region contains additional peaks at 223.0 and 227.6 eV corresponding to S 2s core level and attributed respectively to S²⁻ of MoS₂ and to S₂²⁻ species from MoO_xS_y oxysulfide.

Results reported in Table 6 show that Mn addition clearly influences the formation of the different Mo phases. First of all, the addition of Mn to Al₂O₃ leads to a lower proportion of fully sulfided MoS₂ phase when increasing the Mn amount up to 0.5 mol% (as MnO). For instance, the MoS₂ proportion decreases from 76% for the NiMo/Al₂O₃-S reference to 59% for NiMo/AlMn0.5-S. This lower tendency to obtain the fully sulfided MoS₂ phase is accompanied by an increasing formation of the partially sulfided molybdenum oxysulfide phase from 9% for NiMo/Al₂O₃-S to 32% for NiMo/AlMn0.5-S.

However, at higher Mn contents (NiMo/AlMn1-S and NiMo/AlMn2-S), this evolution is reversed with an increase of the MoS₂ proportion to 74% for NiMo/AlMn1-S. It should be noted that this sudden reversed evolution coincides with the appearance of a Mn XPS signal at these higher Mn contents. This result therefore confirms that a high Mn amount favors again the sulfidation of the NiMo catalyst in agreement with the high S/(Ni + Mo) atomic ratio found for NiMo/AlMn1-S and NiMo/AlMn2-S. The nature of Mn after sulfidation can be better ascertained if one considers the

Table 7

Density of stacks per 1000 nm², average stacking number (\bar{N}) and average stack length (\bar{L}) of catalysts.

Catalyst	Stacks per nm ²	\bar{N}	\bar{L} (nm)
NiMo/Al ₂ O ₃ -S	10.0	1.55	2.79 ± 0.27
NiMo/AlMn0.1-S	11.5	1.58	2.80 ± 0.28
NiMo/AlMn0.5-S	10.0	1.63	2.65 ± 0.25
NiMo/AlMn1-S	13.8	1.39	2.83 ± 0.26
NiMo/AlMn2-S	11.4	1.41	2.47 ± 0.23

Mn 2p_{1/2} binding energy values found at high Mn contents. These values range between 653.5 and 653.7 eV and correspond to the formation of the α -MnS phase after sulfidation [43,44]. It should be noted that the low Mn amount detected by XPS is insufficient to impact significantly the evaluation of the S/(Ni + Mo) atomic ratio. Moreover, the presence of an overlapping Ni LMN Auger peak avoids any determination of the Mn amount using the Mn 2p_{3/2} signal.

Results about the decomposition of the Ni 2p core level spectra are also reported in Table 6. The Ni 2p_{3/2} spectra contain three contributions with their respective satellites [22,33,45–48]. The peak at a binding energy of ~852.7 eV is related to NiS_x species. The signals at ~853.8 eV and ~855.4 eV are associated to the NiMoS phase and NiO_x species, respectively. Adding manganese to Al₂O₃ also influences the proportion of promoted NiMoS phase to be formed. The Mn addition first leads to a net decrease of the proportion of the promoted phase for the NiMo/AlMn0.1-S catalyst. At higher Mn contents (NiMo/AlMn0.5-S and NiMo/AlMn1-S cases), the influence of Mn is less marked with only a slight decrease of the proportion of the NiMoS phase. However, contrary to results acquired about the Mn 3d core level spectra, the main effect is observed here at the highest Mn content analyzed by XPS (NiMo/AlMn2-S) with a net decrease of the NiMoS proportion to about 40%. On the opposite, the amount of non-promoted NiS_x species increases to 45%. Finally, the proportion of nickel oxide remains more or less constant whatever the Mn content. This lower formation of the promoted phase for NiMo/AlMn2-S corresponds to the appearance of a higher amount of Mn³⁺ species, particularly after calcination, able to react with nickel to form the NiMnO spinel phase (Table 4). This leads to a loss of nickel unable after sulfidation to be used for promoting MoS₂. This point will be more discussed during the evaluation of the catalytic properties.

3.3.2. Transmission electron microscopy

TEM analyses were performed in order to evaluate the influence of Mn on the morphology and dispersion of the MoS₂ slabs. Representative images of NiMo/Al₂O₃-S, NiMo/AlMn0.1-S, NiMo/AlMn0.5-S, NiMo/AlMn1-S and NiMo/AlMn2-S catalysts are shown in Fig. 10A–E respectively. Statistical determination of the stacking number and slab length of MoS₂ particles were performed on several TEM images taken on different regions of micrographs.

The NiMo/Al₂O₃-S catalyst presents typical fringes of the MoS₂ phase (Fig. 10A) with a relatively homogeneous dispersion of MoS₂ particles and with a superficial density of 10.0 stacks per 1000 nm² (Table 7). The addition of manganese up to 0.5 mol% Mn (as MnO) does not modify significantly the average slab length and stacking degree of the MoS₂ particles by comparison to the NiMo/Al₂O₃-S reference. Increasing further the Mn amount as for NiMo/AlMn1-S however leads to less stacked slabs than for lower Mn contents but with similar average slab length. This leads to a redispersion of the MoS₂ particles on the support surface and therefore to a higher superficial density of stacks per nm². In the case of NiMo/AlMn2-S, similar average slab length as for NiMo/AlMn1-S is found while a significant decrease in average slab length is now observed (2.47 nm vs 2.79 nm for the NiMo/Al₂O₃-S reference). This lower stacking degree and/or smaller slab length coincides once

again with the reappearance of a Mn contribution on the support surface suggesting that Mn enhances the dispersion of the active phase through a higher interaction between MoS₂ slabs and the support.

3.4. Dibenzothiophene hydrodesulfurization on the NiMo sulfide catalysts supported on AlMn_x supports

The influence of manganese added to sol–gel Al₂O₃ for preparing NiMo/AlMn_x catalysts has been evaluated using the hydrodesulfurization of dibenzothiophene (DBT). The HDS of DBT leads through two parallel reaction pathways to two main products, biphenyl (BP) along the so-called direct desulfurization (DDS) route and cyclohexylbenzene (CHB), obtained along the hydrogenating (HYD) route [49]. Under our conditions, BP is not hydrogenated into CHB.

Results are reported in Table 8. Depending on the Mn content used, the hydrodesulfurization properties change strikingly for the different NiMo catalysts that were prepared. First of all, it should be noted that all the NiMo catalysts, whatever the Mn content, present a high selectivity in BP along the DDS pathway. About activity results, adding low contents of manganese does not modify apparently the activity of the resulting NiMo catalysts up to a Mn amount of 0.5 mol% (as MnO). The NiMo/AlMn0.5-S catalyst indeed presents a rate constant only 10% higher than for the NiMo/Al₂O₃-S reference prepared without manganese. The situation changes when increasing the Mn content as for NiMo/AlMn1-S with this time, the highest rate constant observed for all NiMo catalysts ($44.3 \times 10^{-7} \text{ mol g}_{\text{cat}}^{-1} \text{ s}^{-1}$) about 50% higher than for the reference solid. Finally, increasing further the amount of Mn as for NiMo/AlMn2-S leads to a strong depleting effect with an activity 23% lower than for the non-Mn containing reference. The activity remains low afterwards with an even lower rate constant for NiMo/AlMn5-S. This negative effect observed at high Mn content can be explained easily by the lowest proportion of the promoted NiMoS phase as observed by XPS for NiMo/AlMn2-S (Table 6).

4. Discussion

In order to go deeper in the understanding of how manganese influences hydrodesulfurization properties, it is necessary to determine the evolution of the intrinsic HDS activity through determination of turnover frequency (TOF) values. TOF values are calculated considering the geometrical model developed for MoS₂ slabs [50]. This model allows determining the total number of Mo atoms in the slabs and the number of edge atoms (Mo_e) active in HDS using the following equations:

$$\text{Mo}_t = 3n^2 + 3n + 1$$

$$\text{Mo}_e = 6n$$

with $n(\text{\AA}) = L/(2 \times 3.2)$ (L = slab length, and $d_{\text{Mo-Mo}} = 3.2 \text{\AA}$).

Correlation with XPS Mo 3d decomposition results then leads to the determination of the number of Mo^{IV} edge sites. Turnover frequency (TOF) values in h⁻¹ (Table 8) are then calculated as follows:

$$\text{TOF}(\text{h}^{-1}) = r \cdot N / n_{(\text{MoS}_2\text{e})}$$

with r , the DBT activity at 320 °C, N the Avogadro number and $n_{(\text{MoS}_2\text{e})}$ the number of Mo edge atoms as MoS₂.

Using such an approach, it can be observed that the addition of low Mn content (0.1 and 0.5 mol% Mn as MnO) already leads to a significant increase of the TOF values by about 35% compared to the NiMo/Al₂O₃-S reference. This shows that even if a lower proportion of fully sulfided MoS₂ phase is obtained for NiMo/AlMn0.1-S and NiMo/AlMn0.5-S (Table 6), this is compensated by a higher

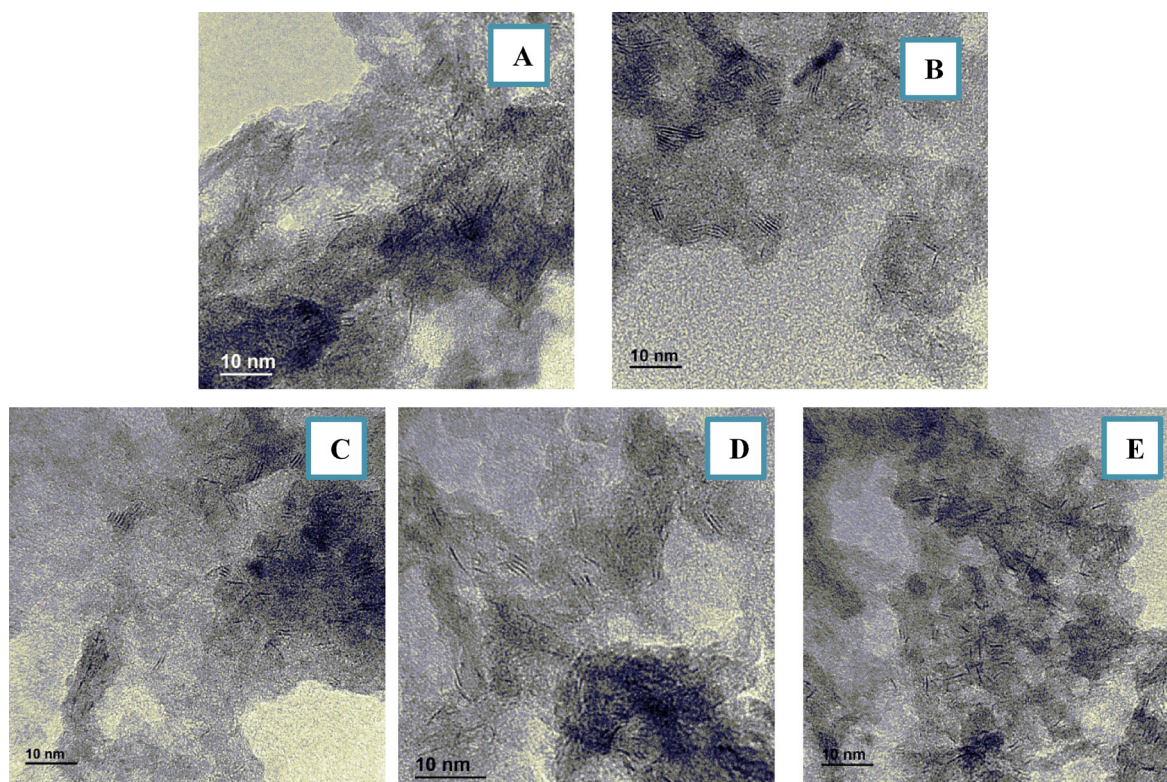


Fig. 10. Representative TEM images of (A) NiMo/Al₂O₃-S, (B) NiMo/AlMn0.1-S, (C) NiMo/AlMn0.5-S, (D) NiMo/AlMn1-S and (E) NiMo/AlMn2-S catalysts.

Table 8

DBT hydrosulfurization results ($P = 30$ bars H₂, 500 ppmS) of the NiMo catalysts supported on AlMn_x supports. Comparison to the NiMo/Al₂O₃ reference. T° reaction: 320 °C, LHSV = 4.2 h⁻¹.

Catalyst	Conversion (%)	$r \times 10^{-7}$ (mol s ⁻¹ ·g _{cat})	BP selectivity (%)	TOF (h ⁻¹)	[NiMoS] (10 ⁻⁴ mol _{Ni} /g _{cat})	Ni (in NiMoS)/Mo(edge)
NiMo/Al ₂ O ₃ -S	44	30.1	97	44.8	2.22	0.70
NiMo/AlMn0.1-S	47	33.6	97	59.6	1.75	0.54
NiMo/AlMn0.5-S	46	33.1	98	61.1	2.09	0.64
NiMo/AlMn1-S	57	44.3	97	72.8	1.84	0.62
NiMo/AlMn2-S	36	23.2	95	36.5	1.52	0.45
NiMo/AlMn5-S	32	20.9	97	–	–	–

intrinsic activity of the remaining sulfide active sites. A possible reason for such an effect is related to the influence of manganese species at the oxide state on the nature of the Mo oxides formed and their interaction with the Al₂O₃ support. Indeed, as shown by UV-vis DR spectroscopy (Figs. 4 and 5), the addition of low Mn content favors the formation of Mn²⁺ species mainly in interaction with the Al₂O₃ support. Since Mn²⁺ species cannot interact strongly with Mo and Ni species, this would decrease the support interaction between Mn-Al₂O₃ and Ni/Mo oxide species limiting the formation of Mo-O-Al linkages [51–55]. The disruption of Mo-O-Al linkages would lead after sulfidation to MoS₂ slabs in weaker interaction with the Al₂O₃ support. This also influences the intrinsic activity of the NiMoS phase formed. Indeed, Candia et al. [51] proposed that for promoted MoS₂ catalysts, two types of phases could exist: (1) a type I phase in strong interaction with a support and poorly HDS active and (2) a very active type II phase in weak or lack of interaction with the support. The Type I phase would be particularly favored on alumina support by Mo-O-Al linkages while the type II phase would be observed on more weakly interacting supports. The weaker support interaction induced by Mn²⁺ species then favors a higher intrinsic activity of the resulting NiMoS active sites. This point will be discussed later. It should also be noted however that Mn is no longer present here after sulfidation (Table 5). This “burying” process limits the beneficial effect

resulting from the presence of Mn²⁺ species in interaction with the support and limits the sulfidation rate of the final catalysts as confirmed later when considering the NiMo/AlMn1-S catalyst. Finally, the nature of the Mo oxide species formed (MoO₄²⁻ for NiMo/AlMn0.1 or Mo₇O₂₄⁶⁻ for NiMo/AlMn0.5) does not influence strongly the final dispersion of the MoS₂ slabs after sulfidation. Indeed, similar average slab lengths and stacking degrees are found in both cases (Table 7). Therefore, up to a polymerization degree corresponding to Mo₇O₂₄⁶⁻ species, there is no clear effect on the final dispersion of the MoS₂ particles. It should however be noted that contrary to MoO₄²⁻, the formation of Mo₇O₂₄⁶⁻ species favors the formation of partially sulfided molybdenum oxysulfides after activation.

The increase of the Mn content up to 1 mol% Mn (as MnO) leads to a significant increase of the TOF for the corresponding NiMo/AlMn1-S catalyst with a rate constant value 60% higher than for the NiMo/Al₂O₃-S reference. In this case, neither an effect on the dispersion of MoS₂ particles nor a change in the nature of the Mn species formed influencing the support interaction can be envisaged. About dispersion, the same Mo₇O₂₄⁶⁻ species are formed in the present case (Table 4) as for NiMo/AlMn0.5-S showing that increasing the Mn content to 1 mol% Mn (as MnO) does not influence significantly the nature of the Mo oxide species formed. This leads after sulfidation once again to similar aver-

age slab length as for the previous case. Similarly, the manganese species in interaction with Al_2O_3 formed at the oxide state are Mn^{2+} or Mn^{4+} known to poorly interact with Mo and Ni species. The main change observed here when increasing the Mn content to 1 mol% Mn as MnO is related to the reappearance of a Mn signal as observed by XPS (Table 5) resulting in a higher sulfidation rate of the corresponding NiMo catalysts and to less stacked MoS_2 slabs (Table 7). This direct influence of Mn on the final HDS properties of NiMo/ Al_2O_3 catalysts was already observed in our previous study using Mn- Al_2O_3 support but prepared by impregnation of Al_2O_3 by manganese acetate [56]. This result is also in agreement with the only study reported in the literature about NiMnMo/ Al_2O_3 catalyst [28,57] showing a synergetic effect on the NiMo activity resulting from the addition of Mn.

Finally, increasing further the Mn content to 2 mol% (as MnO) leads to a strong decrease of the TOF value by about 20% compared to the NiMo/ Al_2O_3 -S reference. This is directly related to the formation of Mn^{3+} species in high amount reacting with Ni to form the NiMnO spinel phase (Table 4). This loss of nickel not available anymore to decorate MoS_2 slabs results in a lower proportion of the promoted NiMoS phase (Table 6) and therefore in a lower intrinsic activity. It should also be noted that the formation mainly of highly polymerized $\text{Mo}_8\text{O}_{26}^{4-}$ species leads to smaller MoS_2 slabs than in previous cases (2.5 nm vs 2.7–2.8 for the preceding cases (Table 7). However, this higher MoS_2 dispersion is insufficient to compensate the loss of promoted active sites resulting from the formation of the NiMnO spinel phase.

XPS, TEM, and elemental analysis can also be used to evaluate the number of moles of Ni engaged in NiMoS moieties by multiplying the percentage of NiMoS found by XPS by the Ni content determined by ICP-OES (Table 8). Results show systematically a lower amount of NiMoS entities in the NiMo/AlMn_x catalysts compared to the NiMo/ Al_2O_3 -S reference. Up to NiMo/AlMn1-S and taking into account the higher TOF values found for these Mn-containing catalysts, it confirms a higher intrinsic activity of the NiMoS entities on Mn-containing catalysts related to a lower support interaction and to a direct Mn influence. Similarly, the proportion of Ni in NiMoS entities in decoration of Mo edge atoms can be evaluated by dividing the moles of Ni in NiMoS entities by the Mo edge amount determined using TEM measurements (Table 8). Once again, the proportion of nickel in decoration of Mo edge atoms remains lower for NiMo/AlMn_x catalysts than for the reference confirming that if a lower proportion of promoted sites are formed when Mn is used, their intrinsic activity is higher than for the reference solid prepared without Mn.

Finally, as expected, for NiMo/AlMn2-S, the lowest amount of NiMoS entities and Ni decoration of Mo edge atoms are found emphasizing the strong negative impact due to the formation of the NiMnO spinel phase induced by Mn^{3+} species.

5. Conclusions

The present study shows a beneficial effect of adding manganese to an Al_2O_3 support prepared by the sol–gel technique for preparing NiMo catalysts used for hydrodesulfurization applications. Results show a direct link between the oxidation state of Mn species during the drying and calcination steps, its influence on the Mo oxide species formed, and the final sulfide active phase.

The use of low manganese concentrations (0.1 and 0.5 mol%) allows to keep manganese mainly as Mn(II) in interaction with Al_2O_3 . The relative inertness of Mn(II) toward Ni and Mo allows decreasing the interaction between the Al_2O_3 support and the sulfide active phase increasing the intrinsic activity of the promoted NiMoS entities. However, the higher intrinsic activity of the promoted sites found in this case does not compensate the fact that

a lower amount of these NiMoS entities are formed. This is also related to the fact that after sulfidation, in this case, Mn is not present anymore at the catalyst surface. Indeed, Mn in close interaction with MoS_2 favors a higher sulfidation rate of the NiMo catalysts.

This fact is clearly observed when increasing the Mn content to 1 mol%. In this case, the reappearance of Mn at the catalyst surface leads to a better sulfidation rate and to the highest TOF value. Keeping Mn in interaction with Al_2O_3 , mainly as Mn(II) or Mn(IV) at the oxide state, also contributes to a higher intrinsic activity of the NiMoS phase. Finally, a direct positive synergetic effect induced by Mn cannot be excluded.

At too high Mn content (5 mol%), Mn^{3+} species form in high amount. These species react with nickel to form the NiMnO spinel phase resulting in a loss of Ni not available anymore to form a promoted NiMoS phase.

Acknowledgements

The authors gratefully acknowledge for their support the ECOS Nord program referenced M16P01 mainly financed by the French Embassy in Mexico. Also, the authors appreciate the support of ANUIES-CONACYT program with reference number 275186.

Appendix A. Supplementary data

Supplementary data associated with this article can be found, in the online version, at <http://dx.doi.org/10.1016/j.apcatb.2017.04.058>.

References

- [1] S.T. Oyama, Y.K. Lee, *J. Catal.* 258 (2008) 393–400.
- [2] G. Berhault, Metal sulfides: novel synthesis methods and recent developments, in: V.I. Parvulescu, E. Kemnitz (Eds.), *New Materials for Catalytic Applications*, Elsevier, 2016, pp. 313–360.
- [3] S.K. Bej, S.K. Maity, U.D. Turaga, *Energy Fuels* 18 (2004) 1227–1237.
- [4] T.C. Ho, J.M. McConnachie, *J. Catal.* 277 (2011) 117–122.
- [5] L. Van Haandel, M. Bremmer, P.J. Kooyman, J.A.R. Van Veen, T. Weber, E.J.M. Hensen, *ACS Catal.* 5 (2015) 7276–7287.
- [6] S. Eijsbouts, L.C.A. van den Oetelaar, R.R. van Puijenbroek, *J. Catal.* 229 (2005) 352–364.
- [7] Y. Fan, H. Xiao, G. Shi, H. Liu, Y. Qian, T. Wang, G. Gong, X. Bao, *J. Catal.* 279 (2011) 27–35.
- [8] A. Guevara-Lara, R. Bacaud, M. Vrinat, *Appl. Catal., A* 328 (2007) 99–108.
- [9] C. Thomazeau, V. Martin, P. Afanasiev, *Appl. Catal., A* 199 (2000) 61–72.
- [10] M.D. Romero, J.A. Calles, A. Rodriguez, J.C. Cabanellas, *Ind. Eng. Chem. Res.* 37 (1998) 3846–3852.
- [11] M. Breyse, J.L. Portefaix, M. Vrinat, *Catal. Today* 10 (1991) 489–505.
- [12] J.A. Cecilia, A. Infantes-Molina, E. Rodríguez-Castellón, A. Jiménez-López, *J. Phys. Chem. C* 113 (2009) 17032–17044.
- [13] Y. Sakashita, *Surf. Sci.* 489 (2001) 45–58.
- [14] R.G. Leliveld, A.J. van Dillen, J.W. Geus, D.C. Koningsberger, *J. Catal.* 171 (1997) 115–129.
- [15] N. Topsøe, H. Topsøe, *J. Catal.* 84 (1983) 386–401.
- [16] G. Murali Dhar, B.N. Srinivas, M.S. Rana, M. Kumar, S.K. Maity, *Catal. Today* 86 (2003) 45–60.
- [17] W. Chen, F. Maugé, J. van Gestel, H. Nie, D. Li, X. Long, *J. Catal.* 304 (2013) 47–62.
- [18] E. Altamirano, J.A. De Los Reyes, F. Murrieta, M. Vrinat, *J. Catal.* 235 (2005) 403–412.
- [19] F. Rashidi, T. Sasaki, A.M. Rashidi, A.N. Kharat, K.J. Jozani, *J. Catal.* 299 (2013) 321–335.
- [20] Usman, T. Kubota, I. Hiromitsu, Y. Okamoto, *J. Catal.* 247 (2007) 78–85.
- [21] Y. Li, D. Pan, C. Yu, Y. Fan, X. Bao, *J. Catal.* 286 (2012) 124–136.
- [22] J.C. Mogica-Betancourt, A. López-Benítez, J.R. Montiel-López, L. Massin, M. Aouine, M. Vrinat, G. Berhault, A. Guevara-Lara, *J. Catal.* 313 (2014) 9–23.
- [23] K. Fujisawa, M. Nabika, *Coord. Chem. Rev.* 257 (2013) 119–129.
- [24] S. Velu, N. Shah, T.M. Jyothi, S. Sivasanker, *Microporous Mesoporous Mater.* 33 (1999) 61–75.
- [25] R. Radhakrishnan, S.T. Oyama, Y. Ohminami, K. Asakura, *J. Phys. Chem. B* 105 (2001) 9067–9070.
- [26] N. Stamatik, K. Goundani, J. Vakros, K. Bourikas, C. Kordulis, *Appl. Catal., A* 325 (2007) 322–327.
- [27] C.M.S. Polato, A.C.C. Rodrigues, J.L.F. Monteiro, C.A. Henriques, *Ind. Eng. Chem. Res.* 49 (2010) 1252–1258.

- [28] T.C. Ho, *Catal. Today* 130 (2008) 206–220.
- [29] A.D. Gandubert, C. Legens, D. Guillaume, S. Rebours, E. Payen, *Surf. Interface Anal.* 38 (2006) 206–209.
- [30] P.C. Yen, Y.S. Huang, K.K. Tjong, *J. Phys.: Condens. Matter* 16 (2004) 2171–2180.
- [31] Y. Okamoto, T. Imanaka, S. Teranishi, *J. Catal.* 65 (1980) 448–460.
- [32] T. Weber, J.C. Muijsers, J.H.M.C. van Wolput, C.P.J. Verhagen, J.W. Niemantsverdriet, *J. Phys. Chem.* 100 (1996) 14144–14150.
- [33] T.K.T. Ninh, L. Massin, D. Laurenti, M. Vrinat, *Appl. Catal., A* 407 (2011) 29–39.
- [34] E. Payen, R. Hubaut, S. Kasztelan, O. Poulet, J. Grimblot, *J. Catal.* 147 (1994) 123–132.
- [35] Z. Contreras-Valdez, J.C. Mogica-Betancourt, A. Alvarez-Hernandez, A. Guevara-Lara, *Fuel* 106 (2013) 519–527.
- [36] G. Leofanti, M. Padovan, G. Tozzola, B. Venturelli, *Catal. Today* 41 (1998) 207–219.
- [37] R.J. Hunter, Zeta potential in colloid science: principles and applications, in: R.H. Ottewill, R. Rowell (Eds.), *Colloid Science Series*, Academic Press, London, 1981.
- [38] M. Kosmulski, *J. Colloid Interface Sci.* 353 (2011) 1–15.
- [39] W.S. Kijlstra, E.K. Poels, A. Blik, B.M. Weckhuysen, R.A. Schoonheydt, *J. Phys. Chem. B* 101 (1997) 309–316.
- [40] R.S. Weber, *J. Catal.* 151 (1995) 470–474.
- [41] H. Hu, I.E. Wachs, *J. Phys. Chem.* 99 (1995) 10911–10922.
- [42] I. Alstrup, I. Chorkendorff, R. Candia, B.S. Clausen, H. Topsøe, *J. Catal.* 77 (1982) 397–409.
- [43] J. Lu, P. Qi, Y. Peng, Z. Meng, Z. Yang, W. Yu, Y. Qian, *Chem. Mater.* 13 (2001) 2169–2172.
- [44] Y. Xin, L.Y. Cao, J.F. Huang, J. Liu, J. Fei, C.Y. Yao, *J. Alloys Compd.* 549 (2013) 1–5.
- [45] C. Roukoss, D. Laurenti, E. Devers, K. Marchand, L. Massin, M. Vrinat, *C.R. Chim* 12 (2009) 683–691.
- [46] L. Coulier, G. Kishan, J.A.R. van Veen, J. Niemantsverdriet, *J. Phys. Chem. B* 106 (2002) 5897–5906.
- [47] L. Blanchard, J. Grimblot, J.P. Bonnelle, *J. Catal.* 98 (1986) 229–234.
- [48] J.P. Espinós, A.R. González-Elipé, G. Munuera, *Solid State Ionics* 63–65 (1993) 748–754.
- [49] M. Breyse, G. Berhault, S. Kasztelan, M. Lacroix, F. Maugé, G. Perot, *Catal. Today* 66 (2001) 15–22.
- [50] S. Kasztelan, H. Toulhoat, J. Grimblot, J.P. Bonnelle, *Appl. Catal.* 13 (1984) 127–159.
- [51] R. Candia, O. Sorensen, J. Villadsen, N.Y. Topsøe, B.S. Clausen, H. Topsøe, *Bull. Soc. Chim. Belg.* 93 (1984) 763–773.
- [52] E. Diemann, Th. Weber, A. Müller, *J. Catal.* 148 (1994) 288–303.
- [53] E.J.M. Hensen, V.H.J. de Beer, J.A.R. van Veen, R.A. van Santen, *Catal. Lett.* 84 (2002) 59–67.
- [54] R.G. Leliveld, A.J. van Dillen, J.W. Geus, D.C. Koningsberger, *J. Catal.* 165 (1997) 184–196.
- [55] G. Berhault, M. Perez De la Rosa, A. Mehta, M.J. Yácaman, R.R. Chianelli, *Appl. Catal., A* 345 (2008) 80–88.
- [56] A. López-Benítez, G. Berhault, A. Guevara-Lara, *J. Catal.* 344 (2016) 59–76.
- [57] T.C. Ho, *Catal. Today* 98 (2004) 3–18.